Draft version March 28, 2024
Typeset using LaTeX default style in AASTeX631

The relative prevalence of wave-packets and coherent structures in the inertial and kinetic ranges of turbulence as seen by Solar Orbiter

Alina Bendt,[1] Sandra Chapman ,[1, 2, 3] and Thierry Dudok de Wit[2, 4]

[1]Centre for Fusion, Space And Astrophysics, Physics Department, University of Warwick, UK
[2]International Space Science Institute, Bern, Switzerland
[3]Department of Mathematics and Statistics, University of Tromso, Norway
[4]University of Orléans

Submitted to ApJ

ABSTRACT

The Solar Orbiter (SO) mission provides the opportunity to study the evolution of solar wind turbulence. We use SO observations of nine extended intervals of homogeneous turbulence to determine when turbulent magnetic field fluctuations may be characterized as: (i) wave-packets and (ii) coherent structures (CS). We perform the first systematic scale-by-scale decomposition of the magnetic field using two wavelets known to resolve wave-packets and discontinuities, the Daubechies 10 (Db10) and Haar respectively. The probability distributions (pdfs) of turbulent fluctuations on small scales exhibit stretched tails, becoming Gaussian at the outer scale of the cascade. Using quantile-quantile plots, we directly compare the wavelet fluctuations pdfs, revealing three distinct regimes of behaviour. Deep within the inertial range (IR) both decompositions give essentially the same fluctuation pdfs. Deep within the kinetic range (KR) the pdfs are distinct as the Haar wavelet fluctuations have larger variance and more extended tails. On intermediate scales, spanning the IR-KR break, the pdf is composed of two populations: a core of common functional form containing $\sim 97\%$ of fluctuations, and tails which are more extended for Haar fluctuations than Db10 fluctuations. This establishes a crossover between wave-packet (core) and CS (tail) phenomenology in the IR and KR respectively. The range of scales where the pdfs are 2-component is narrow at 0.9 au ($4-16$ s) and broader ($0.5-8$ s) at 0.4 au. As CS and wave-wave interactions are both candidates to mediate the turbulent cascade, these results offer new insights into the distinct physics of the IR and KR.

Keywords: Solar Orbiter (SO), solar wind, turbulence, intermittency, wavelets, coherent structures

1. INTRODUCTION

The super Alfvenic, high Reynolds number solar wind flow provides a large scale natural laboratory for plasma turbulence (see e.g. Tu & Marsch (1995); Bruno & Carbone (2013); Chen (2016); Marino & Sorriso-Valvo (2023)). There are extensive observations at 1 au (e.g. from ACE, WIND and Cluster) principally around the $L1$ point upstream of earth (for a review see e.g. Bruno & Carbone (2013); Verscharen et al. (2019)). Until recently, observations at different distances from the sun have been provided by e.g. Ulysses and Voyager (see e.g. Bruno & Carbone (2013); Nicol et al. (2008); Cuesta et al. (2022); Yordanova et al. (2009); Bourouaine et al. (2012); Maruca et al. (2023); Pagel & Balogh (2003)). Solar Orbiter (Müller et al. 2013, 2020) and Parker Solar Probe offer new opportunities to study the solar wind at different distances from the sun from 1 au to within 0.1 au.

Results around 1 au consistently show features of turbulence phenomenology. The power spectrum of magnetic field fluctuations in the trace and components exhibits a well defined inertial range (IR) of magneto-hydrodynamic (MHD) turbulence with a steeper kinetic range (KR) scaling below ion scales and a shallower, approximately $1/f$-range at larger scales (e.g. Kiyani et al. (2015)). The IR trace power spectrum typically exhibits a power spectral scaling around $-5/3$ (e.g. Matthaeus & Goldstein (1982); Beresnyak (2012); Podesta et al. (2007)), which corresponds to the Kolmogorov 1941 (K41) scaling (Kolmogorov et al. 1997). Closer to the sun, at distances smaller than 0.4 au (e.g. Šafránková et al. (2023); Chen et al. (2020); Lotz et al. (2023)) the power spectrum on average evolves towards a spectral slope of $-3/2$, which corresponds to Iroshnikov-Kraichnan (IK) scaling

(Iroshnikov 1963). Below ion kinetic scales the spectrum steepens to a well defined kinetic range (e.g. Sahraoui et al. (2009); Chen et al. (2014); Verscharen et al. (2019); Kiyani et al. (2013)). The steeper kinetic range power spectrum corresponds to an increase in compressibility (Kiyani et al. 2009, 2013; Alexandrova et al. 2008, 2013) compared to the IR.

Both waves and coherent structures are features of MHD turbulent phenomenology (Tu & Marsch 1995; Frisch 1995) and may mediate the turbulent cascade. Recent studies of the KR reveal whistler waves, ion-cyclotron waves, and kinetic Alfvén waves as well as coherent structures in this regime (e.g. Roberts et al. (2017); Sahraoui et al. (2009); Wu et al. (2013); Zhou et al. (2023); Alexandrova et al. (2013); Chhiber et al. (2021); Osman et al. (2012a); He et al. (2011); Salem et al. (2012)), where kinetic effects and ultimately dissipation become important (e.g. Kiyani et al. (2015); Verscharen et al. (2019)). A feature of turbulence, is intermittency, which has been identified by Koga et al. (2007) as arising from phase correlation among different scales due to nonlinear wave-wave interactions and as coherent structures by Gomes et al. (2022); Camussi & Guj (1997) and Veltri (1999). These coherent structures have also been identified as localized sites of turbulent dissipation (Perri et al. 2012; Greco et al. 2017; Wu et al. 2013; Osman et al. 2012a, 2014, 2012b; Sioulas et al. 2022a).

Identification of turbulence rests upon statistical characterization, since quantitative aspects of turbulence are reproducible in a statistical sense and each realization is distinct (Frisch 1995; Tu & Marsch 1995). A key characteristic of turbulence is scale-by-scale similarity (Frisch 1995; Tu & Marsch 1995). The process of statistical characterization and testing for scaling is to (i) obtain the fluctuation time-series decomposition, by differencing, Fourier (Welch 1967) or wavelet decomposition (Farge 1991; Meneveau 1991; Daubechies 1990; Mallat 1989); (ii) analyse the fluctuations scale by scale by examining power spectra and pdfs. All the above methods are in widespread use in the study of solar wind turbulence (eg. Podesta et al. (2007); Kiyani et al. (2013); Camussi & Guj (1997); Farge (1992); Yamada & Ohkitani (1991a); Do-Khac et al. (1994); Narasimha (2007); Bolzan et al. (2009); Beresnyak (2012); Bruno & Carbone (2013); Chapman & Hnat (2007); Katul et al. (2001)).

Turbulent fluctuations in solar wind data extracted by differencing the time-series have non-Gaussian probability distributions (pdfs) (Bruno & Carbone 2013; Frisch 1995; Tu & Marsch 1995; Alexandrova et al. 2008; Bruno et al. 2004, 2003; Sorriso-Valvo et al. 1999; Hnat et al. 2003) which tend to become more Gaussian on scales approaching the outer scale of the turbulent cascade. The stretched exponential tails of the pdfs (Hnat et al. 2003), hereafter referred to as stretched tails, show that large fluctuations have a higher probability of occurrence than for a Gaussian distribution, consistent with intermittency (Bruno (2019) and references therein).

In this paper, we will perform the first systematic comparison between decompositions focused on (i) coherent structures, namely differencing the time-series (as implemented in structure functions), formally equivalent to a Haar wavelet decomposition and (ii) wave-packets, that is Fourier and wavelet decompositions. Different time-series decompositions extract different features in the time-series (Schneider & Farge 2001; Farge 1991, 1992). We will see that comparing different decompositions of the time-series can identify how coherent structures and wave-wave interactions contribute to the turbulent cascade.

The IR of solar wind turbulence is anisotropic due to the presence of a background magnetic field (Matthaeus et al. 1990) as seen in the power spectrum (e.g. Bruno & Carbone (2013); Oughton et al. (2015); Bandyopadhyay & McComas (2021); Chen et al. (2011); Horbury et al. (2008); Wicks et al. (2010)). The background field that is expected to order the anisotropy of the magnetic fluctuations can be defined globally, averaging across scales and time, or locally, scale-by-scale and varying in time (e.g. Horbury et al. (2008); Beresnyak (2012); Chapman & Hnat (2007); Duan et al. (2021); Kiyani et al. (2013); Podesta (2009); Turner et al. (2012); Zhang et al. (2022); Yamada & Ohkitani (1991b)). In this paper we will consider the former, global background field. Averaging the magnetic field vector over a global timescale exceeding that of the centre scale of the turbulence defines a global background field. Together with the time-averaged solar wind velocity, a coordinate system is constructed. The time average is typically taken over the entire intervals of data (in this study we use intervals from 10 to 3.15 h length) (Bruno & Carbone 2013).

In this paper we will find that the IR-KR transition can, depending upon conditions, coincide with the crossover to a region where coherent structures dominate the population of large fluctuations. By comparing different decompositions of the time-series in a global background field, we find that coherent structures are prevalent in the KR and less dominant in the IR. The temporal scale where the PSD steepens from the IR to the KR is indicative of a transition from MHD to ion kinetic physics. There has been considerable effort to identify this scale break, and it does not necessarily appear at the same scale for any plasma conditions (Chen et al. 2014; Markovskii et al. 2008; Wang et al. 2018; Šafránková et al. 2023). Generally, the spectral break occurs between 0.02 – 4 Hz (Markovskii et al. 2008). Recently, Šafránková et al. (2023) found that the spectral break decreases with heliocentric distance from around 4 Hz close to the sun to 0.1 Hz around 1 au.

This paper is organised in three sections. In section 2 we present the data intervals analysed and data analysis methods. In section 3 we present a systematic comparison of power spectra and fluctuation pdfs applied to two different scale-by-scale decompositions of the data. We conclude in section 4.

2. DATA AND METHODS

2.1. *Data*

We analyse in detail the time-series of magnetic field data from the Magnetometer (MAG) (Horbury et al. 2020) and obtain averaged parameters from the solar wind velocity, density, pressure and temperature measurements of the Solar Wind Analyser (SWA-PAS) (Owen et al. 2020) on board Solar Orbiter (Müller et al. 2013). The solar wind velocity and magnetic field measurements are provided in RTN coordinates, with the magnetic field measurements at a cadence of 8 Hz. We select nine over 10 h long intervals of turbulence which contain homogeneous solar wind flow without any shocks, current sheet crossings and other large events, at heliocentric distances R of $\sim 0.3, 0.6$, and ~ 0.9 au. Three intervals have a plasma $\beta \geq 1.7$. The average solar wind velocity of the intervals, V_{sw} is 494 km s^{-1}. Table 1 presents the intervals, grouped in four categories: i) the high plasma beta of $\beta \geq 2$ intervals from 2021-11-18 at 0.9 au and 2023-03-14 at 0.6 au, ii) this encompasses the interval with a large field alignment angle θ, iii) intervals close to the sun and, iv) intervals at ~ 0.9 au with moderate plasma β. We rotate the magnetic field from RTN coordinates into coordinates ordered by the global time-averaged background field, averaged over the entire interval B_0. The orthogonal coordinate system then has the magnetic field projected onto a component $B_{\|}$ parallel to B_0, and onto perpendicular components $B_{\perp(V_{sw},B)} = B_{\|} \times V_{sw}$, and $B_{\perp(V_{sw}\times B)} = B_{\|} \times B_{\perp(V_{sw},B)}$.

interval [Y-M-D]	**length** [h]	R [au]	$\mathbf{V_{sw}}$ [km s^{-1}]	$\tau_{\mathbf{adv}}$ [h]	β	$\rho_{\mathbf{i}}$ [Hz]	**KR break** [Hz]	θ [°]
2022-01-01	~ 14 h	0.997 au	584 km s^{-1}	70.96 h	1.36	0.31 Hz	0.5 Hz	27.14°
2022-01-03	~ 15.3 h	0.992 au	530 km s^{-1}	77.68 h	1.55	0.19 Hz	0.5 Hz	31.82°
2022-01-04	~ 10.75 h	0.989 au	438 km s^{-1}	93.87 h	0.95	0.24 Hz	0.25 Hz	18.07°
2022-01-06	~ 24 h	0.984 au	312 km s^{-1}	130.94 h	1.79	0.23 Hz	0.5 Hz	64.51°
2021-11-18	~ 14.75 h	0.934 au	533 km s^{-1}	72.82 h	2.08	0.19 Hz	1 Hz	160.93°
2023-03-14	~ 10 h	0.597 au	548 km s^{-1}	45.27 h	2.48	0.68 Hz	1 Hz	68.63°
2022-03-18	~ 12 h	0.369 au	414 km s^{-1}	37.08 h	0.98	1.35 Hz	1 Hz	7.29°
2022-04-04	~ 24 h	0.369 au	555 km s^{-1}	27.64 h	0.76	1.22 Hz	1 Hz	16.82°
2022-04-01	~ 31.5 h	0.344 au	535 km s^{-1}	26.66 h	1.02	1.75 Hz	1 Hz	21.46°

Table 1. Table of the nine interval characteristics: the date, length, heliocentric distance R, average solar wind speed V_{sw}, advection times τ_{adv}, plasma β, ion-gyro frequency ρ_i, the KR-IR spectral break time scale and the field alignment angle θ. R is quoted to three significant figures to distinguish intervals very close to each other, while the other parameters (except V_{sw}) are quoted to two decimal places.

2.2. *Wavelet decompositions of the time-series and intermittency measures*

We decompose the magnetic field time-series of these nine intervals of homogeneous turbulence using two different discrete wavelet transforms, the Daubechies 10 (Db10) and Haar wavelet (the latter is equivalent to differencing of the time-series). The different wavelets are designed to resolve wave-like features and sharp changes in the time-series respectively (Farge 1992; Percival & Walden 2000; Torrence & Compo 1998; Daubechies 1990). Fourier, wavelet and differencing (structure functions) have all been used extensively in the study of solar wind turbulence, especially in testing for statistical scaling (e.g. Podesta et al. (2007); Kiyani et al. (2013); Farge (1992); Yamada & Ohkitani (1991a); Do-Khac et al. (1994); Narasimha (2007); Bolzan et al. (2009); Chapman & Hnat (2007); Katul et al. (2001)). Wavelet decompositions are time-frequency localized and therefore are well suited to isolating wave-packets and coherent structures (Daubechies 1990; Farge et al. 1996). Wavelet transforms sample the frequency space logarithmically which is well suited to the determination of the power law exponent of the power spectrum (Mallat 1989). Wavelet transforms decompose the signal (here a component of the magnetic field) at each scale into detail and approximation time-series. The details capture the fluctuations in the field, while the approximations are a running average (Farge 1992; Percival & Walden 2000).

We will use τ to denote the scale of decomposition and t_k as discrete time for the magnetic field time-series denoted as $B(t)$. The wavelet details $\delta B_{\tau,t_k}$ at a time-scale $\tau = 2^j\Delta$, where Δ is the sampling period, and $j \in \mathbf{Z}$ the scale, and t_k the location of the magnetic field $B(t)$ are (Farge et al. 1996)

$$\delta B_{\tau,t_j} = \sum_{k=1}^{N} B(t_k)\,\sqrt{\tau}\Psi(\tau t_k - t_j)\,, \tag{1}$$

where N is the length of the data set and $\Psi_{j,i}$ is the set of wavelets. The power spectrum can then be defined as (Farge 1992; Schneider & Farge 2001)

$$E(t', \tau) = \frac{2\Delta}{N} |\delta B_{\tau,t_j}|^2 \ . \tag{2}$$

The Haar wavelet H is a step-function $H_{j,k}(x) = 2^{j/2} H(2^j x - k)$ (Nickolas 2017). Since the Haar wavelet shape corresponds to sharp changes it will be sensitive to coherent structures. The Daubechies 10 wavelet (Db10) is determined from a base wavelet with 10 wavelet coefficients (Daubechies 1992; Percival & Walden 2000) and its shape corresponds to that of wave-packets. The Db10 wavelet has a higher number of vanishing moments than the Haar wavelet, enabling a more accurate determination of steeper power law exponents in the kinetic range (Farge et al. 1996). The Haar wavelet is only suited for determining slopes ≥ -3 (Cho & Lazarian 2009). The wavelet transform is performed by the MATLAB Maximum Overlap Discrete Wavelet Transform (MODWT) (noa 2022a) with reflected boundaries.

3. RESULTS

We obtain scale-by-scale decompositions of the 9 intervals using both Haar and Db10 wavelets, which then provide estimates of the power spectra and the fluctuation pdfs and their moments scale-by-scale. The aim is twofold: (i) to verify that the selected intervals do indeed exhibit properties consistent with turbulence phenomenology; (ii) by comparing the results of these analyses for the Haar (that is time-series differences) and the Db10 wavelets, to gain new insights into the relative importance of coherent structures and wave-like features at different temporal scales across the turbulent cascade.

3.1. *Power spectra*

We first establish that the power spectral estimates (Figure 1) of the Haar and Db10 discrete wavelets, show a clearly defined inertial range with power spectral breaks at low frequencies to the $1/f$-range and at high frequencies to the kinetic range, consistent with a well developed turbulence cascade. Figure 1 presents the power spectral density (PSD) for a representative interval for all magnetic field components, (a) $B_{\perp(V_{sw},B)}$, (b) $B_{\perp(V_{sw},B)}$, (c) $B_{\|}$. The full set of PSDs for all intervals is presented in Figure A.3. Each spectrum is a single estimate using the full temporal range of each interval and is not averaged. The parallel magnetic field component consistently shows less power than the perpendicular components (e.g. Šafránková et al. (2023)). The intervals closer to the sun overall show more power at all scales (Figure A.4 presents the standard deviation of the wavelet fluctuations for all intervals), as previously observed by Chen et al. (2020). A slight curvature in the IR is detected in $B_{\|}$ and close to the sun, the latter is consistent with active development of the turbulence with increasing distance. A curvature in the spectrum is consistent with extended self similarity (Chapman & Nicol 2009) or with an additional spectral break within the IR (Wang et al. 2023). The spectral exponents generally do not present clear IK or K41 scaling but rather values that lie between those values, as also seen by Wang et al. (2023).

As expected, the Haar and Db10 wavelet estimates diverge in the KR, seen in Figure 1, as the Haar cannot resolve scaling exponents steeper than -3 (Cho & Lazarian 2009). However, both the Haar and Db10 spectral estimates, within their given frequency resolution, identify the same location of the spectral break, the smallest scale at which the wavelet PSDs coincide. The IR-KR spectral break scale moves with the larger of the ion scales ρ_i and d_i (blue vertical lines in Figure 1, which is reproduced for all intervals in Figure A.3), decreasing with decreasing distance from $4 - 1$ s and plasma $\beta \ \geq 2$. The evolution of the spectral break was previously observed by Šafránková et al. (2023); Lotz et al. (2023); Bruno & Trenchi (2014) for magnetic field trace spectra. For $B_{\|}$ the spectral break differs by one dyadic scale to the perpendicular components for $\beta \geq 2$ and the interval 2022-01-03 at 0.992 au.

The outer inertial range spectral break to the $1/f$-range (Figure 1) is typically located before the 1 h scale. The early $1/f$-break is most evident in $B_{\|}$ and $B_{\perp(V_{sw},B)}$. The break between the IR and 1/f is well resolved in our wavelet spectral estimates which do not require multi-sample averaging, the break frequency decreases with decreasing distance. This was also reported by Chen et al. (2020), who averaged each interval over a sliding window Fourier magnetic field trace spectra to obtain the break at $\sim 10^4$ s for large and $\sim 10^3$ s for small distances from the sun.

3.2. *Fluctuation PDFs scale by scale*

Turbulence is routinely studied by decomposing the observed time-series into fluctuations on different temporal scales. Here, we compare the fluctuation pdfs extracted by the Haar (identical to differencing), and Db10 wavelets, which resolve discontinuities, and wave-packets, respectively, to discriminate between wave-packets and coherent structures phenomenology at different scales within the turbulence cascade. As we move from the shortest to the longest scales, the fluctuation pdf evolves from a sharply peaked functional form with extended tails to Gaussian-like at the outer scale of the turbulence inertial range (Figure 2

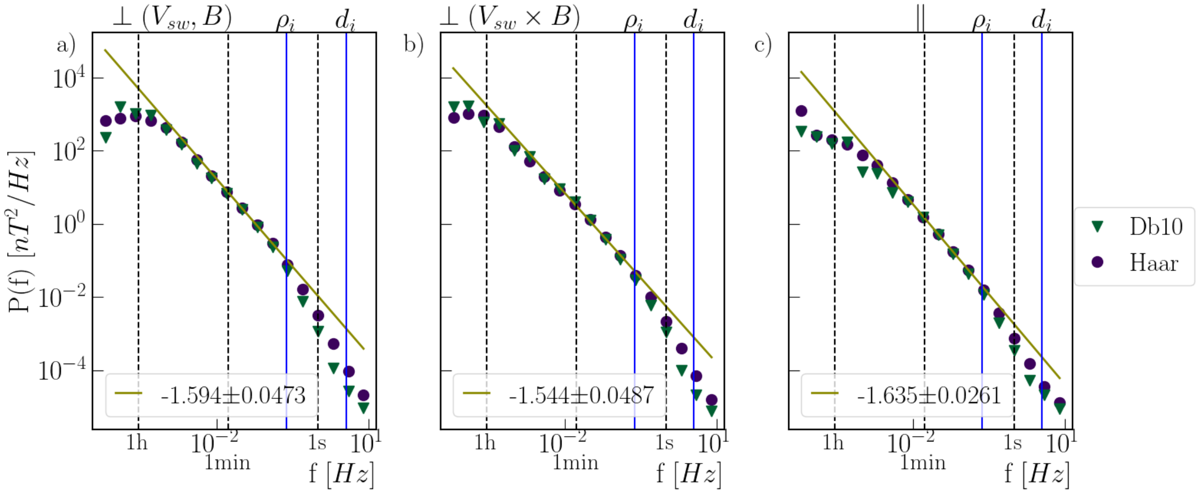

Figure 1. Power Spectral Density (PSD) with clear $1/f$, inertial and kinetic ranges in both Haar and Db10 wavelets. PSD are shown for one representative interval for each magnetic field component (column) and the respective scaling exponent in the inertial range fitted on the Haar wavelet. The interval is at 0.989 au with $\beta = 0.95$ and $\theta = 18.07°$ from 2022-01-04. The Db10 wavelet is shown by green triangles, purple circles are the Haar wavelet. Blue vertical lines denote the ion-gyro frequency ρ_i and ion-inertia length d_i. Dashed black vertical lines denote scales marked on the x-axis as 1 s, 2 s, 1 min, 1 h. Yellow fit lines to the Haar wavelet power spectrum show the spectral exponent, which is quoted to three significant figures.

presents the Haar wavelet pdfs and Figure 3 the Db10 wavelet pdfs) (Bruno et al. 2004; Alexandrova et al. 2008; Frisch 1995; Tu & Marsch 1995). The overall amplitude of the fluctuations, captured by their standard deviation, grows with temporal scale in a manner consistent with power-law scaling in the power spectral density (Figure A.4 compares the standard deviation of the wavelet fluctuation pdfs for all intervals). Specific coherent structures have been found to lie within the stretched tails of the fluctuation distributions (Bruno (2019) and references therein). Coherent structures have been identified as origins of intermittency and sites of dissipation (e.g. Osman et al. (2012b,a); Greco et al. (2017); Veltri (1999); Gomes et al. (2022)). This confirms that the selected intervals are exhibiting the typical characteristics of turbulent fluctuations.

In Figure 4 we directly compare the fluctuation pdfs of the two wavelet decompositions across scales spanning the KR and IR. A full set of the fluctuation pdfs of both wavelet decompositions is provided in Figures A.5, A.6 and A.7 for each magnetic field component. Four different intervals are shown in Figure 4 (rows) where the heliocentric distance decreases from top to bottom. The scales (columns in Figure 4) shown are at 0.25, 0.5, 2 and 8 s. We find that three different morphologies of the pdfs can be seen in Figure 4. In the KR (columns 1 and 2) the Haar (green circles) and Db10 (purple circles) fluctuation extremes, or tails, diverge. The Haar fluctuation pdf exhibits more stretched and extended tails than the Db10 decomposition. Deep in the IR (column 4) there is a well-defined distribution core where the Haar and Db10 extracted fluctuation pdfs coincide. This core is between the blue vertical lines (column 4) whereas in the KR two distinct pdfs are found. On intermediate scales (column 3) the pdfs have two components: The core of the fluctuation pdfs overlap, whereas the tails of the wavelet pdfs diverge. The Haar wavelet tails are more extended than those of the Db10 wavelet. The intermediate crossover range generally spans the spectral break scale obtained from the PSD. This suggests three different regimes of turbulence: i) consistent with coherent structures in the kinetic range, ii) consistent with wave-packets deep in the inertial range, where the wavelet pdfs overlap and, iii) a crossover regime on intermediate scales, where a two component pdf is observed with tails consistent with coherent structures.

The distribution functions may differ either in their functional form, in their moments, or both. We can discriminate this with compensated Quantile-Quantile (QQ)-plots (Wilk & Gnanadesikan 1968; Easton & McCulloch 1990; Tindale & Chapman 2017) of the wavelet fluctuation pdfs (see section A.1.1 for a description of Quantile-Quantile plots). If the Haar and Db10 pdfs are drawn from the same distribution, then the compensated quantile trace will be a horizontal straight line at zero. If the pdfs are drawn from the same functional form but with different variance, the quantile trace will be a straight line diagonally. A non-linear relationship on the QQ-plot indicates that the two distributions have different functional forms.

Figure 5 plots compensated QQ-plots which directly compare the Haar and Db10 fluctuation pdfs for four example intervals (rows) for each magnetic field component (columns). We have normalised the wavelet fluctuations by the overall magnetic field

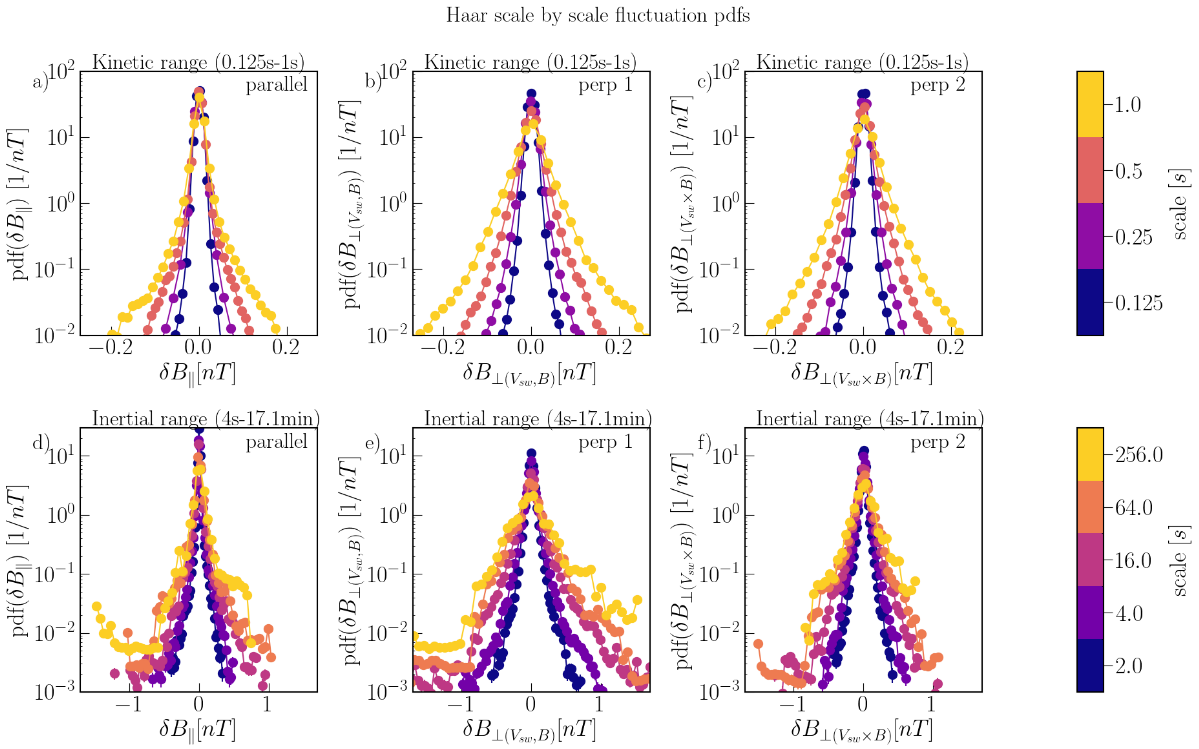

Figure 2. Probability distribution functions (pdfs) of Haar wavelet fluctuations developing from stretched-tailed KR pdfs to Gaussian-like outer scale pdfs. Pdfs are shown for each component (columns) of the magnetic field for the KR (top row, panels a) to c)) up to 1 s and IR (bottom row, panels d) to f)) for the interval at 0.989 au from 2022-01-04. The colour marks the scale with largest scale in yellow and smallest scale in blue. The number of bins is scaled by the standard deviation σ at the corresponding scale and bins with less than 10 counts are discarded. The error is estimated as $\sqrt{n}$, where n is the bin count, error bars are too small to be resolved visually.

magnitude of each interval. Each colour refers to the fluctuations at a given temporal scale, the largest scale in purple at 64 s and the smallest scale at 0.25 s in teal. A full set of QQ-plots for all intervals is provided in Figure A.8.

In the KR scales (0.25, 0.5 s in Figure 5) the quantiles lie on a single line along $y = Ax$. This single diagonal line thus shows that the Haar wavelet pdf has a larger variance than the Db10 wavelet pdf but the same functional form. This difference in variance between the two pdfs A decreases with increasing scale, the slope of the quantiles trace becomes less steep. On average the variance obtained from the Haar fluctuation pdfs is larger than that obtained from the Db10 fluctuation pdfs at kinetic range scales. In the IR scales in Figure 5 (1 s and larger) the quantile trace has a central region which lies along $y = 0$ so that the Haar and Db10 wavelet pdfs are similar in this central core. The largest fluctuations depart from this and form a distinct tail; more large fluctuations are obtained by the Haar decomposition than from the Db10 decomposition. The IR distributions are thus of a 2-component character with a central core distribution, where the wavelets have the same functional form and variance, and tails of same underlying functional form with different variance where the Haar decomposition resolves larger amplitude fluctuations. Blue vertical lines (column 3) in Figure 5 for 8 s denote the limits of the core. These points are also marked in Figure 4 (column 4). At 8 s about 97 % of the fluctuations are within the core distribution between the blue lines. At 64 s there is a small increase to an average of 98.5 %.

Within this overall behaviour there are differences depending on the heliocentric distance and field alignment angle θ. At 0.9 au, $\beta = 2.08$ and $\theta = 160.93°$ (panels e) to f)) the pdfs exhibits an abrupt crossover where at 1 s (the spectral break) a core appears containing 97 % of the fluctuations, which does not expand with increasing scale. This abrupt crossover is not seen for the other high β interval (panels h) and i)) and thus is associated here with the large θ. For intervals $R \leq 0.4$ au a core is seen at 0.5 s containing about 92 % of fluctuations in the core. The crossover range ends at 8 s for $R \leq 0.6$ au and at 16 s for $R \sim 0.9$ au. The crossover range is thus broader at small distances from the sun than at larger distances.

The first column in Figure 5 shows the $B_{\parallel}$ component with the KR scales consistently as single line where the Haar wavelet fluctuation pdfs has larger amplitude tails and with increasing scale the core expands and the amplitude of the tails of the Haar

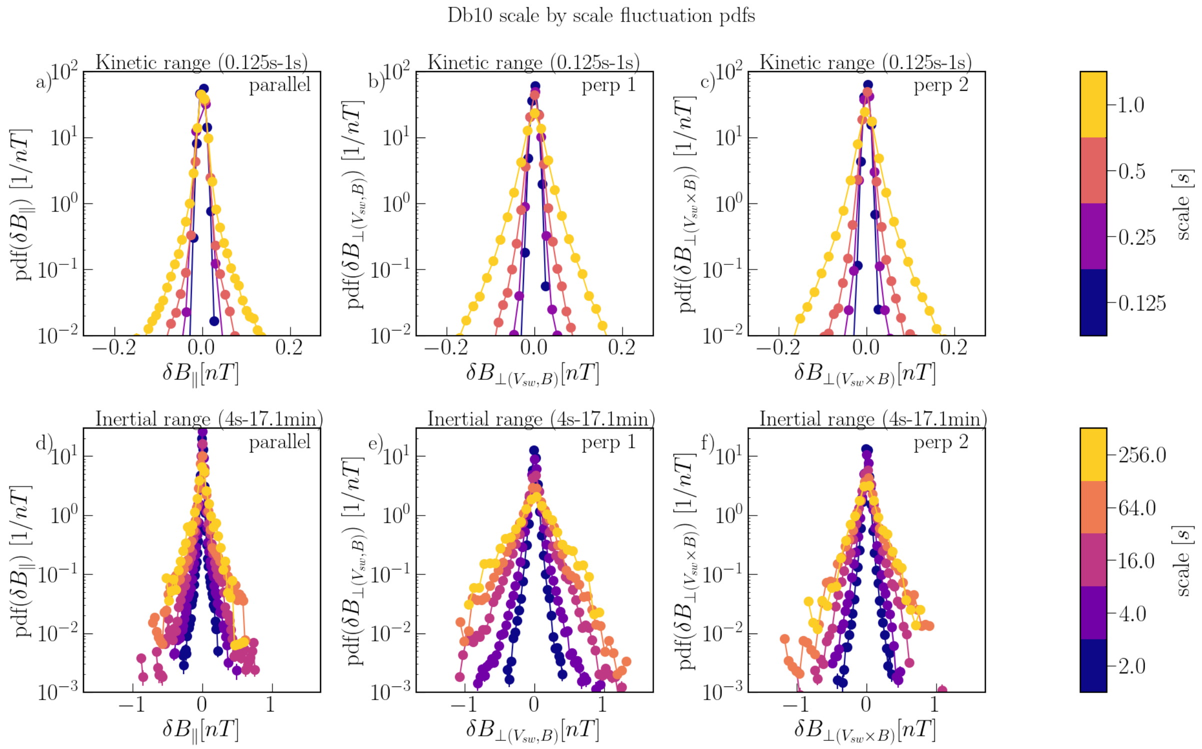

Figure 3. Probability distribution functions (pdfs) of Db10 wavelet fluctuations developing from stretched-tailed KR pdfs to Gaussian-like outer scale pdfs. Pdfs are shown for each component (columns) of the magnetic field for the KR (top row, panels a) to c)) up to 1 s and IR (bottom row, panels d) to f)) for the interval at 0.989 au from 2022-01-04. The colour marks the scale with largest scale in yellow and smallest scale in blue. The number of bins is scaled by the standard deviation σ at the corresponding scale and bins with less than 10 counts are discarded. The error is estimated as $\sqrt{n}$, where n is the bin count, error bars are too small to be resolved visually.

wavelet fluctuation pdf decreases. At 0.597 au and large β (row 3) the distributions show a mixture of behaviours, with $B_{\perp(V_{sw}\times B)}$ exhibiting the same evolution as intervals close to the sun, and $B_{\perp(V_{sw},B)}$ like intervals at larger distances.

In summary, given that the Haar wavelet decomposition preferentially resolves coherent structures when compared to the Db10 wavelet, these results show that the KR is dominated by coherent structures across all amplitudes of fluctuations, whereas fluctuations in the IR are two component in character, with an extended tail dominated by coherent structures, and a core which can be be consistent with either coherent structures or wave-packets.

4. CONCLUSIONS

We performed scale-by-scale analysis of the magnetic field in a coordinate system ordered by the direction of the global, time-averaged background magnetic field for each of nine intervals of solar wind turbulence seen by SO for different plasma parameters and solar distances. We compared time-series decompositions using the Haar (equivalent to differencing) and Db10 wavelets, which distinguish discontinuities (coherent structure phenomenology) and wave-packets (the phenomenology of wave-wave interactions) respectively. This work presents the first systematic comparison of these methods in the context of solar wind turbulence using wavelet decompositions that specifically characterize wave-like and coherent structure-like features in the time-series. As we move from the shortest to the longest scales, the fluctuation pdf moves from a sharply peaked functional form with extended, super-exponential tails, to Gaussian at the outer scale of the turbulence (Frisch 1995; Camussi & Guj 1997). The overall amplitude of the fluctuations, captured by their standard deviation, grows with temporal scale in a manner consistent with power-law scaling in the power spectral density (Figure A.4). However we find that the fluctuation pdf functional form depends upon the decomposition used to obtain the fluctuations. We directly compared the pdfs of fluctuations obtained from Haar and Db10 wavelet decompositions. We find that the fluctuation pdfs reveal three distinct morphologies

- Deep in the KR, the Haar and Db10 decompositions fluctuations share the same functional form, but the Haar fluctuations have a variance that is larger than that obtained by the db10 by a factor of 4.22 at 0.9 au and 2.195 at 0.3 au, consistent with the phenomenology of coherent structures.

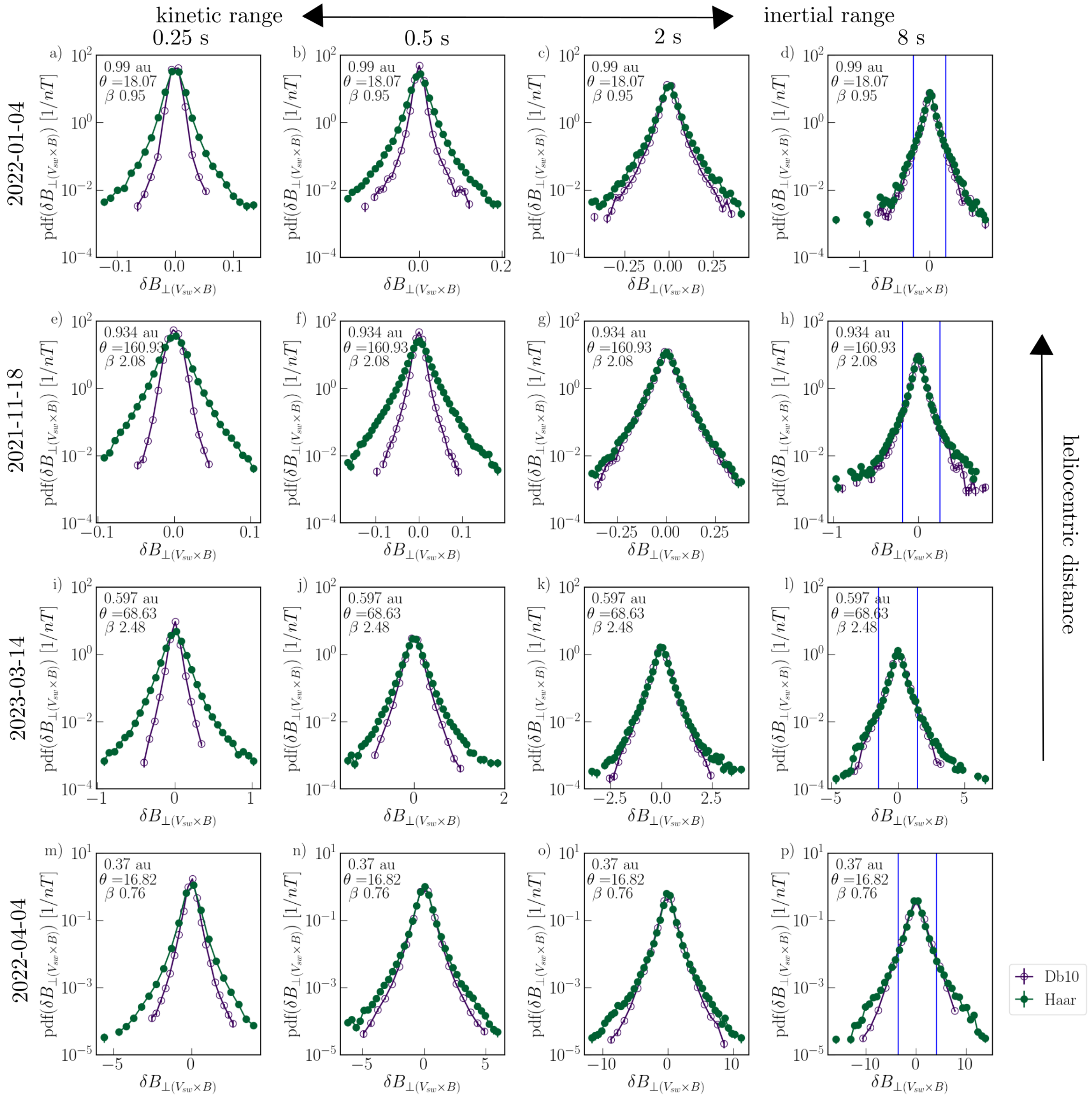

Figure 4. Probability distribution functions (pdfs) comparison between Haar and Db10 wavelet fluctuations. Pdfs are shown for $B_{\perp(V_{sw}\times B)}$ for four example intervals (rows). The chosen intervals (top down) are at 0.989 au with $\beta = 0.95$ and $\theta = 18.07°$, at 0.934 au with $\beta = 2.08$ and $\theta = 160.93°$, at 0.597 au with $\beta = 2.48$ and $\theta = 68.63°$, and at 0.37 au with $\beta = 0.76$ and $\theta = 16.82°$. The scales shown are increasing from left to right at 0.25, 0.5, 2 and 8 s. Filled purple circles are obtained from the Haar wavelet, while green triangles are from the Db10 wavelet.

- Deep in the IR there is a well-defined distribution core where the Haar and Db10 decomposition fluctuation pdfs coincide and have the same functional form. The core contains about 98 % of fluctuations from the 64 s scale.
- At intermediate scales between the IR and KR, the Haar fluctuations form a larger amplitude pdf tail compared to that of the db10 fluctuations. This is consistent with fluctuations in the distribution tails being dominated by coherent structures.
- The intermediate crossover range of scales is located around the IR-KR spectral break scale. The characteristics of this crossover range depend on heliocentric distance and the field alignment angle θ. At distances around 0.9 au the crossover range is quite narrow, from 4 – 16 s. At around 0.3 au the crossover occurs over a broader range of scales from 0.5 – 8 s.

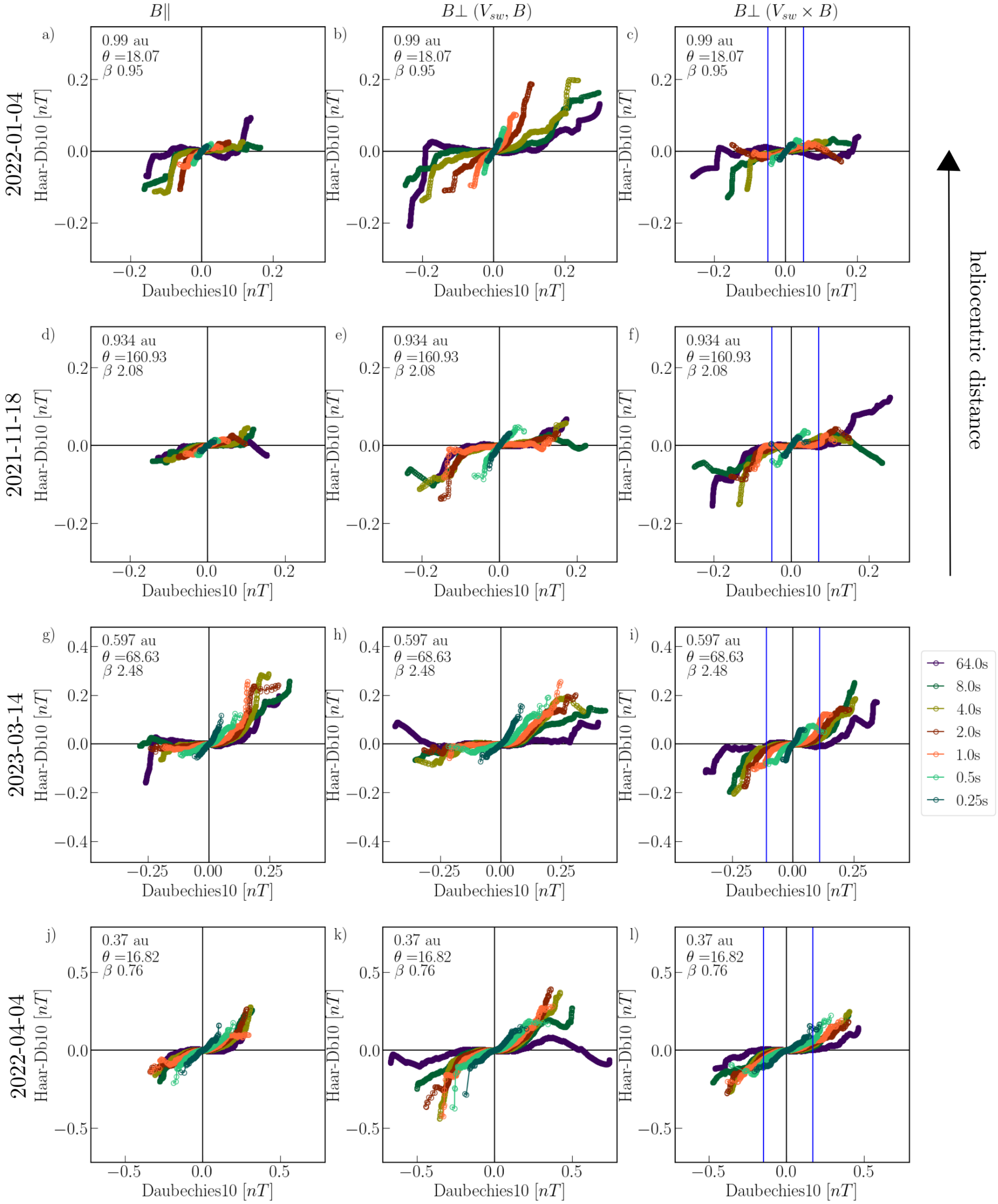

Figure 5. Compensated QQ-Plots compare the functional forms of the wavelet fluctuation pdfs. The compensated QQ-plots are of the $H-Db10$ versus the Db10 wavelet details over-plotted per scale for four intervals (rows) and all magnetic field components (columns). From top to bottom the intervals are at 0.9 au, at 0.9 au with θ = 160.93°, at 0.597 au and β = 2.48, and lastly at 0.3 au. The different scales are denoted with different colours, the largest in purple, the smallest in turquoise. Scales from 0.25 to 8 s and additionally 64 s scales are used. If the quantiles lie on the horizontal black line the distributions are the same.

At a large field alignment angle θ of 160.93° the crossover is abrupt at 1 s and unlike the other cases examined here, the fluctuation pdfs derived from the Haar and db10 decompositions do not fully coincide even at the largest scales of the IR.

Our results highlight the multi-component nature of the pdfs of fluctuations which can arise from either of two distinct phenomenologies that mediate the turbulent cascade, that of wave-packets, and coherent structures. We thus find that the fluctuation pdfs in the KR are consistent with coherent structure phenomenology. Deep in the inertial range the fluctuations pdfs of both wavelet decompositions coincide, which is consistent with either coherent structure or wave-packet phenomenology. On intermediate scales where we find a two-component pdf, the coherent structures dominate the pdf tails.

Additionally, we confirm previously reported results that the IR-KR spectral break typically moves with the larger of the ρ_i and d_i scales depending on distance from the sun and β (Bruno & Trenchi 2014; Lotz et al. 2023; Šafránková et al. 2023; Chen et al. 2014). The power in all components increases with decreasing distance from the sun (Chen et al. 2020). We find that in the KR the two wavelet estimates differ, since the Haar wavelet cannot capture exponents steeper than −3 (Cho & Lazarian 2009; Farge 1991).

In this paper we demonstrate how the Haar and Db10 wavelets resolve different underlying physics. Using the Haar and Db10 wavelets, we have detected a crossover from coherent structure phenomenology in the KR to wave-packet phenomenology in the IR. The crossover behaviour and range of scales depends on the heliocentric distance and field alignment angle. The population of coherent structures at small scales might suggest an association with the dissipation mechanism of turbulence, as suggested by the enhanced heating signatures found near coherent structures (e.g. Osman et al. (2012b); Sioulas et al. (2022a)). A narrower crossover range of scales at large heliocentric distances may be connected to how well the turbulent cascade is developed. The larger range of coherent structures phenomenology at large distances may also be related to the evolution of intermittency with heliocentric distance (e.g. Sioulas et al. (2022b); Bruno et al. (2003); Pagel & Balogh (2003)).

This study only included one interval at large θ and one interval at 0.6 au, which thus may only present outliers. A larger number of intervals at large θ as well as intervals at a variety of distances from the sun should be included in future work. An investigation of the coherent structures and waves present in the respectively dominated scales should give more insight into the physics present and how they connect to each other.

All data used in this study is freely available from the following sources (accessed last on **24th October 2023**): Solar Orbiter Archive.

Solar Orbiter is a mission of international cooperation between ESA and NASA, operated by ESA.

This work is supported by funding for A.Bendt from the Science and Technologies Facilities Council (STFC). A.Bendt also acknowledges support from ISSI. S.C.Chapman acknowledges support from ISSI via the J.Geiss fellowship and AFOSR grant FA8655-22-1-7056 and STFC grant ST/T000252/1. T.Dudok de Wit acknowledges support from CNES.

Software: MatLab (noa 2022a), Scipy (Virtanen et al. 2020), Numpy version 1.23.0 (Harris et al. 2020), Matplotlib version 3.7.1 (Hunter 2007), Astropy (Collaboration et al. 2022), Cdflib https://github.com/MAVENSDC/cdflib

APPENDIX

A. APPENDIX

A.1. *Supporting Methods*

A.1.1. *Quantile-Quantile Plots*

Two distribution functions may differ in their functional form, or in their moments, or both. This difference can be seen in Quantile-Quantile (QQ)-plots (Wilk & Gnanadesikan 1968; Easton & McCulloch 1990; Tindale & Chapman 2017). These QQ-plots are constructed as follows (also see (Wilk & Gnanadesikan 1968; Easton & McCulloch 1990; Tindale & Chapman 2017)). The cumulative density function $C(x)$ gives the likelihood of observing a value of $X \leq x$ as a function of x. The cdf takes values between zero and 1 and defines the quantiles $x(q)$ of the distribution, so that $C(x(q)) = 0.5$ at the value $x(q)$ where $q = 0.5$, the 0.5 quantile, $C(x(q)) = 0.9$ at the value $x(q)$ where $q = 0.9$, the 0.9 quantile and so on. The cdf is inverted to give the quantile function $x(q) = C^{-1}(q)$. The QQ plot then compares the quantile functions of a pair of distributions C_1 and C_2 by plotting x_1 versus x_2 with the quantile q as the parametric coordinate. The resulting QQ-plot has the values of the quantiles of X on the axes of the two distributions to be compared, and the likelihood q as parametric coordinate. This is illustrated in Figure A.1 with two cdfs in panel a) and a compensated QQ-plot in panel b), where the $x_1 - x_2$ is plotted versus x_2 with the quantiles as parametric coordinate

q. With the same functional form, the resulting line of quantiles can take three different shapes: i) if x_1 and x_2 are drawn from the same distribution, then the compensated QQ-plot will be a straight line of $x_2 - x_1 = 0$. ii) if the distribution has a shift in the mean, then it will be a straight line $x_2 - x_1 = c$ shifted from zero by c and iii) if there is a change in the variance, then the compensated QQ-plot will be a straight line at $x_2 - x_1 = x_1$. If the relationship on the QQ-plot is non-linear, the underlying functional forms of the distributions are different. We use the Statistics and Machine Learning Toolbox from MatLab (noa 2022b) to determine the quantiles. In the case of the wavelet fluctuation pdfs, the distributions show three different regimes illustrated with corresponding compensated QQ-plots in Figure A.2: i) the Haar has extended "fatter" tails than the Db10 and the distributions thus differ in σ (panels a and d), ii) the distributions are drawn from the same distributions in the core, but diverge in the tails (panels b and e), iii) the distributions are drawn from the same distributions (panels c and f).

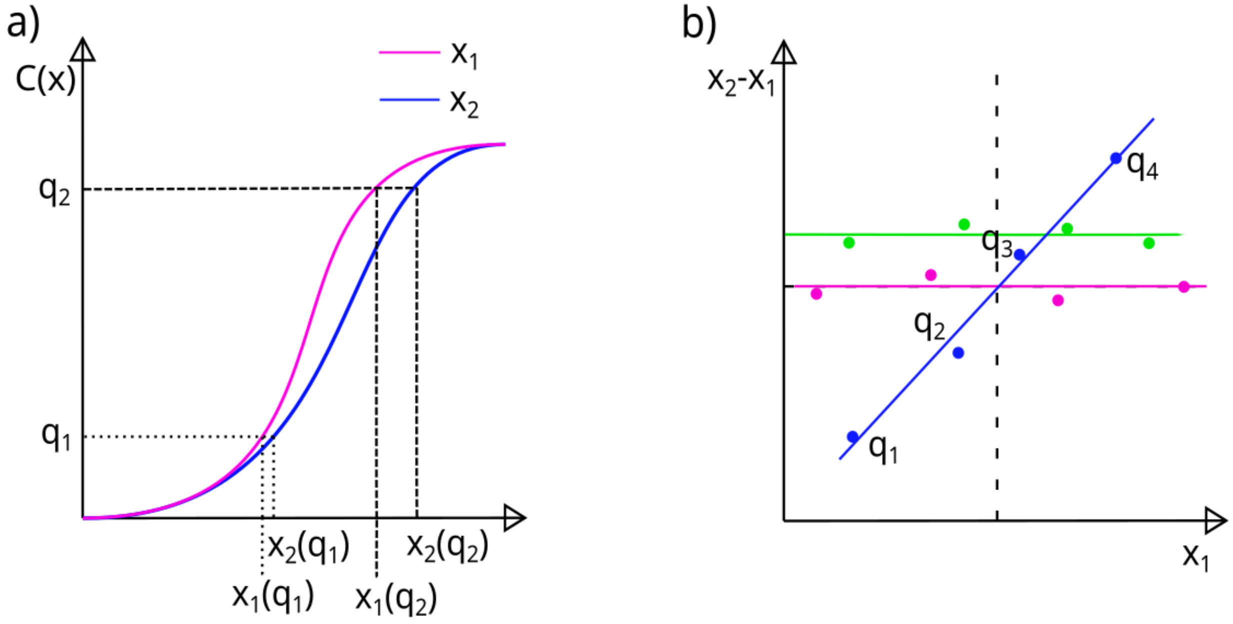

Figure A.1. Diagrams showing the construction of the compensated QQ-plot. (a) The empirical CDFs of the samples x_1 and x_2. Proportion q_1 of the data set is bounded by quantile $x_1(q_1)$ in sample x_1 and quantile $x_2(q_1)$ in sample x_2, similar for q_2. (b) The compensated QQ-plot is produced by plotting $x_1(q)$ against $x_2(q)$ for all values of q. Pink line: $x_2 - x_1 = 0$ i.e. are the same distribution, green line: $x_2 - x_1 = c$ i.e. different mean, blue line: $x_2 - x_1 = x_1$, i.e. different σ.

A.2. *Supporting Figures*

A.2.1. *Power Spectral Measures*

Figure A.3 presents the PSD for all intervals (rows) and each magnetic field component (columns). The increasing power levels are seen from top to bottom rows. The movement of d_i and ρ_i is seen clearly as a continuous shift from $\rho_i > d_i$ at 0.9 au to $d_i > \rho_i$ at 0.3 au. With the lower rows the lower KR break scale is seen as well as a smaller $1/f$-range break.

The second moment of the fluctuation pdfs relates to the PSD by definition and is an indicator for the overall power levels in the fluctuations for each component. Here we plot the standard deviation σ of the fluctuation pdfs versus temporal scale in Figure A.4 for all intervals. As seen in the PSD (Figure 1), the Haar and Db10 wavelet generally agree on the standard deviation in the IR and only significantly diverge at large scales that move towards the upper end of the inertial range. The disagreement in the $1/f$-range is easily seen in the PSD Figure 1 by an early "roll-off" into the $1/f$-range. In terms of overall power there are three distinct groupings of these intervals. At 0.3 au, the intervals show a progressively higher σ compared to the intervals at 0.9 au by a factor of ~ 20 at small scales, reducing to ~ 6 at larger scales. The magnetic field component $B_{\perp(V_{sw},B)}$, has higher σ values than any other component from about 100 s and larger.

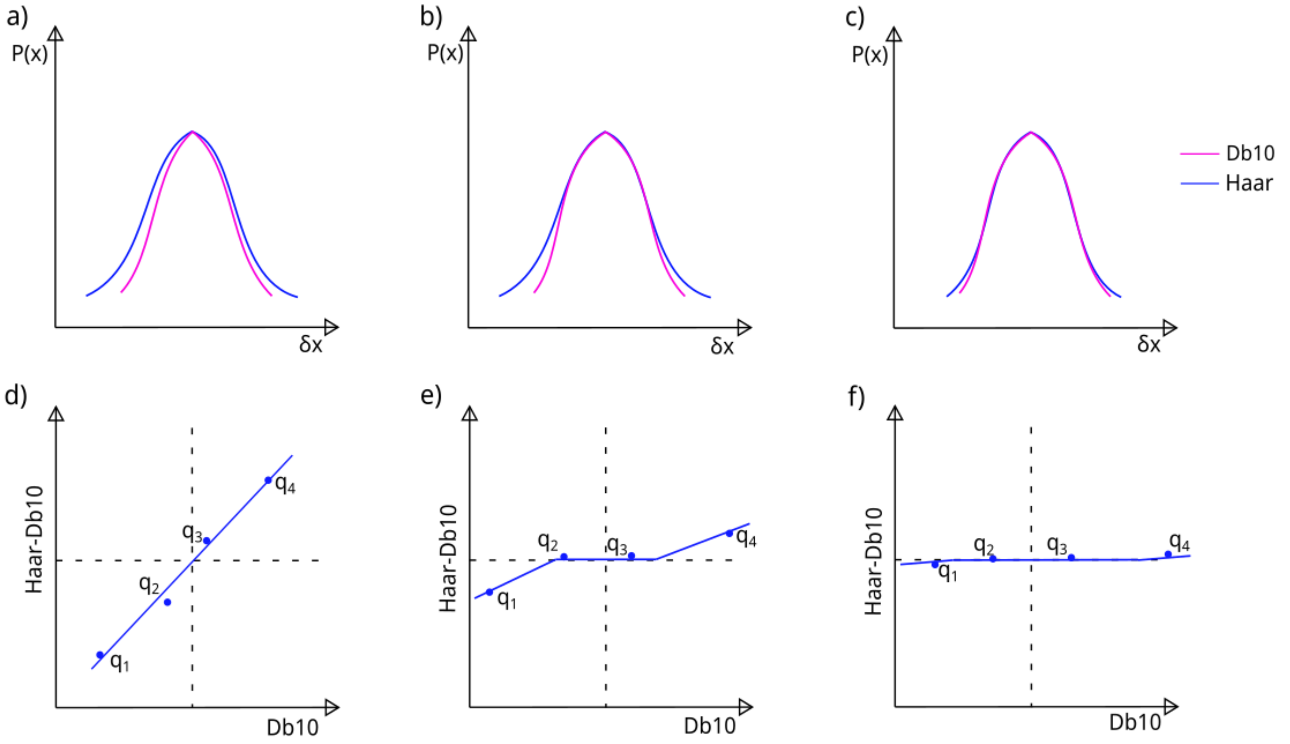

Figure A.2. Diagrams showing the construction of the compensated QQ-plot. (a-c) The pdfs of the samples obtained from Db10 (pink) and Haar (blue) wavelets. (d-f) The compensated QQ-plot of the above pdf.

A.2.2. *Fluctuation distributions*

The following Figures A.5, A.6 and A.7 show the fluctuation pdf comparison between Haar and Db10 wavelets for each interval (row) across scales from 0.25 – 8 and 64 s (columns). The shift of ρ_i (pink circles) and d_i (blue rectangles) is seen, as well as the spectral break in red boxes. The pdfs overlap largely in IR scales, and diverge in the tails in KR scales.

Figure A.8 provides the compensated QQ-plots for all intervals (rows) for each magnetic field component (column). The gradual alignment of the cores is seen for all intervals and for intervals at 0.9 au a single line with differing σ for KR scales is visible, while intervals at smaller distances show an initial core in the KR pdfs. The tails are seen to decrease in slope with increasing scales.

A.2.3. *Time-series*

Figure A.9 displays the time-series sub-intervals and Haar and Db10 decompositions with corresponding acfs for the example interval 2022-01-04 at $\beta = 0.95$ and $\theta = 18.07°$ for all magnetic field components. With increasing scale, the fluctuations become more oscillatory and so does the acf. The Db10 continuously displays a more smooth and oscillatory signal than the Haar wavelet.

REFERENCES

2022a, Wavelet Toolbox version: 6.2 (R2022b) Update 2, Natick, Massachusetts, United States: The MathWorks Inc. https://www.mathworks.com

2022b, Statistics and Machine Learning Toolbox version: 6.2 (R2022b) Update 2 (R2022b) Update 2, Natick, Massachusetts, United States: The MathWorks Inc. https://uk.mathworks.com/help/stats/index.html?s_tid=CRUX_lftnav

Alexandrova, O., Carbone, V., Veltri, P., & Sorriso-Valvo, L. 2008, The Astrophysical Journal, 674, 1153, doi: 10.1086/524056

Alexandrova, O., Chen, C. H. K., Sorriso-Valvo, L., Horbury, T. S., & Bale, S. D. 2013, Space Science Reviews, 178, 101, doi: 10.1007/s11214-013-0004-8

Bandyopadhyay, R., & McComas, D. J. 2021, The Astrophysical Journal, 923, 193, doi: 10.3847/1538-4357/ac3486

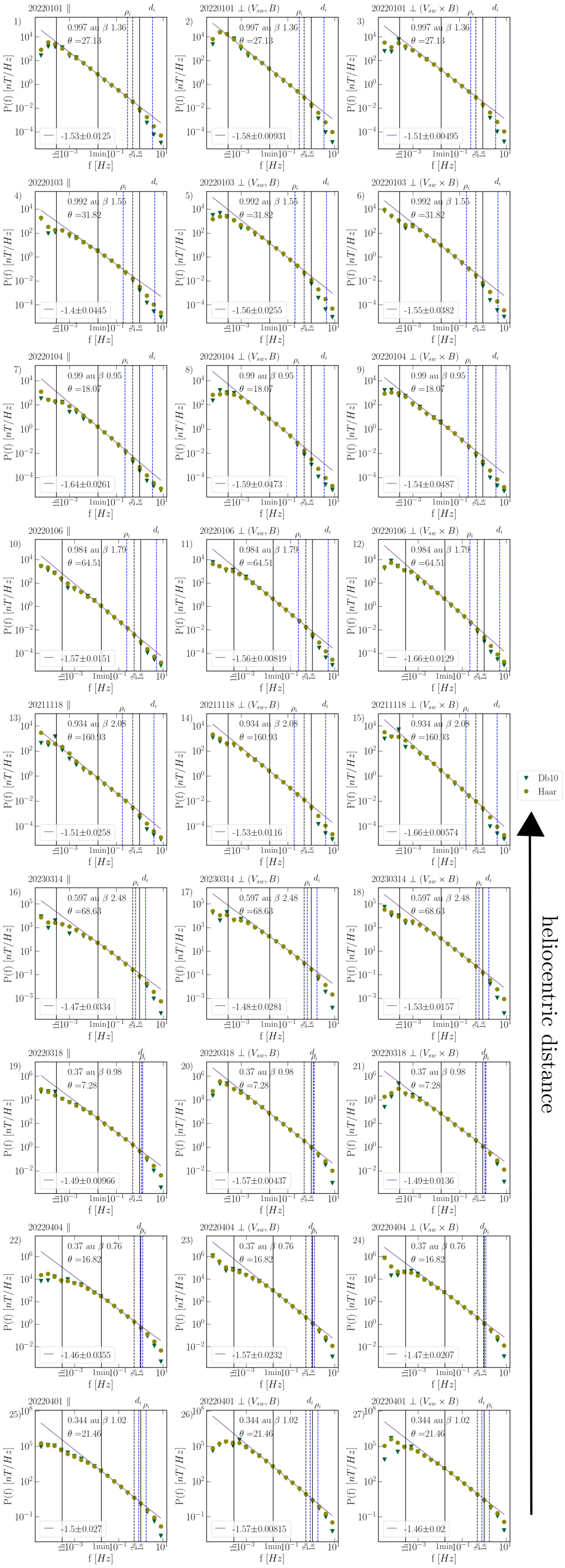

Figure A.3. Power Spectra of all the different intervals (row) with decreasing distance from the sun and for each magnetic field component (column) and the respective scaling exponent in the inertial range fitted on the Haar wavelet. The Daubechies 10 wavelet is shown by green triangles, yellow filled circles are the Haar wavelet. Blue vertical lines denote the ion-gyro frequency ρ_i (dashed) and ion-inertia length d_i (dash-dotted). Black vertical lines denote scales marked on the x-axis as 1 s, 2 s, 1 min, 1 h. Purple fit lines to the Haar wavelet power spectrum show the spectral exponent, which is quoted to three significant figures. Red crosses denote the power spectral estimate of the magnetic field magnitude $|B|$, and an orange line the linear fit to the $|B|$ power law.

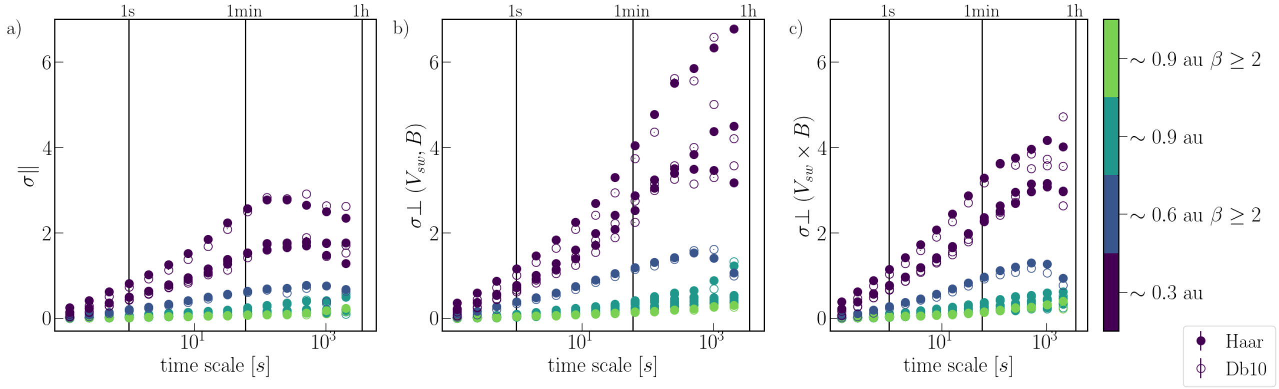

Figure A.4. Comparison of standard deviation with increasing time scales for all intervals per magnetic field component. Open circles mark Daubechies 10 wavelet, while filled circles are for the Haar wavelet of the corresponding colours per interval. The intervals are divided into four different intervals, with intervals at large distances in lighter colours. An early "roll-off" before the 1 h scale is observed in $\sigma_{\|}$, for intervals close to the sun in $\sigma_{\perp(V_{sw},B)}$ and for most intervals in $\sigma_{\perp(V_{sw}\times B)}$. This is due to the early spectral break to the $1/f$-range in the power spectra. The error bars -too small to be seen- were determined by re-sampling and the variation of σ values.

Beresnyak, A. 2012, Monthly Notices of the Royal Astronomical Society, 422, 3495, doi: 10.1111/j.1365-2966.2012.20859.x

Bolzan, M. J. A., Guarnieri, F. L., & Vieira, P. C. 2009, Brazilian Journal of Physics, 39, 12, doi: 10.1590/S0103-97332009000100002

Bourouaine, S., Alexandrova, O., Marsch, E., & Maksimovic, M. 2012, The Astrophysical Journal, 749, 102, doi: 10.1088/0004-637X/749/2/102

Bruno, R. 2019, Earth and Space Science, 6, 656, doi: 10.1029/2018EA000535

Bruno, R., & Carbone, V. 2013, Living Reviews in Solar Physics, 10, doi: 10.12942/lrsp-2013-2

Bruno, R., Carbone, V., Primavera, L., et al. 2004, Annales Geophysicae, 22, 3751, doi: 10.5194/angeo-22-3751-2004

Bruno, R., Carbone, V., Sorriso-Valvo, L., & Bavassano, B. 2003, Journal of Geophysical Research: Space Physics, 108, doi: 10.1029/2002JA009615

Bruno, R., & Trenchi, L. 2014, The Astrophysical Journal Letters, 787, L24, doi: 10.1088/2041-8205/787/2/L24

Camussi, R., & Guj, G. 1997, Journal of Fluid Mechanics, 348, 177, doi: 10.1017/S0022112097006551

Chapman, S. C., & Hnat, B. 2007, Geophysical Research Letters, 34, L17103, doi: 10.1029/2007GL030518

Chapman, S. C., & Nicol, R. M. 2009, Physical Review Letters, 103, 241101, doi: 10.1103/PhysRevLett.103.241101

Chen, C. H. K. 2016, Journal of Plasma Physics, 82, 535820602, doi: 10.1017/S0022377816001124

Chen, C. H. K., Leung, L., Boldyrev, S., Maruca, B. A., & Bale, S. D. 2014, Geophysical Research Letters, 41, 8081, doi: 10.1002/2014GL062009

Chen, C. H. K., Mallet, A., Yousef, T. A., Schekochihin, A. A., & Horbury, T. S. 2011, Monthly Notices of the Royal Astronomical Society, 415, 3219, doi: 10.1111/j.1365-2966.2011.18933.x

Chen, C. H. K., Bale, S. D., Bonnell, J. W., et al. 2020, The Astrophysical Journal Supplement Series, 246, 53, doi: 10.3847/1538-4365/ab60a3

Chhiber, R., Matthaeus, W. H., Bowen, T. A., & Bale, S. D. 2021, The Astrophysical Journal Letters, 911, L7, doi: 10.3847/2041-8213/abf04e

Cho, J., & Lazarian, A. 2009, The Astrophysical Journal, 701, 236, doi: 10.1088/0004-637X/701/1/236

Collaboration, T. A., Price-Whelan, A. M., Lim, P. L., et al. 2022, The Astrophysical Journal, 935, 167, doi: 10.3847/1538-4357/ac7c74

Cuesta, M. E., Parashar, T. N., Chhiber, R., & Matthaeus, W. H. 2022, The Astrophysical Journal Supplement Series, 259, 23, doi: 10.3847/1538-4365/ac45fa

Daubechies, I. 1990, IEEE Transactions on Information Theory, 36, 961, doi: 10.1109/18.57199

—. 1992, Ten lectures on wavelets, CBMS-NSF Regional Conference Series in Applied Mathematics (Society for Industrial and Applied Mathematics). https://epubs.siam.org/doi/10.1137/1.9781611970104

Do-Khac, M., Basdevant, C., Perrier, V., & Dang-Tran, K. 1994, Physica D: Nonlinear Phenomena, 76, 252, doi: 10.1016/0167-2789(94)90263-1

Duan, D., He, J., Bowen, T. A., et al. 2021, The Astrophysical Journal Letters, 915, L8, doi: 10.3847/2041-8213/ac07ac

Easton, G. S., & McCulloch, R. E. 1990, Journal of the American Statistical Association, 85, 376, doi: 10.1080/01621459.1990.10476210

Farge, M. 1991, Physics of Fluids A: Fluid Dynamics, 3, 2029, doi: 10.1063/1.4738850

—. 1992, Annual Review of Fluid Mechanics, 24, 395, doi: 10.1146/annurev.fl.24.010192.002143

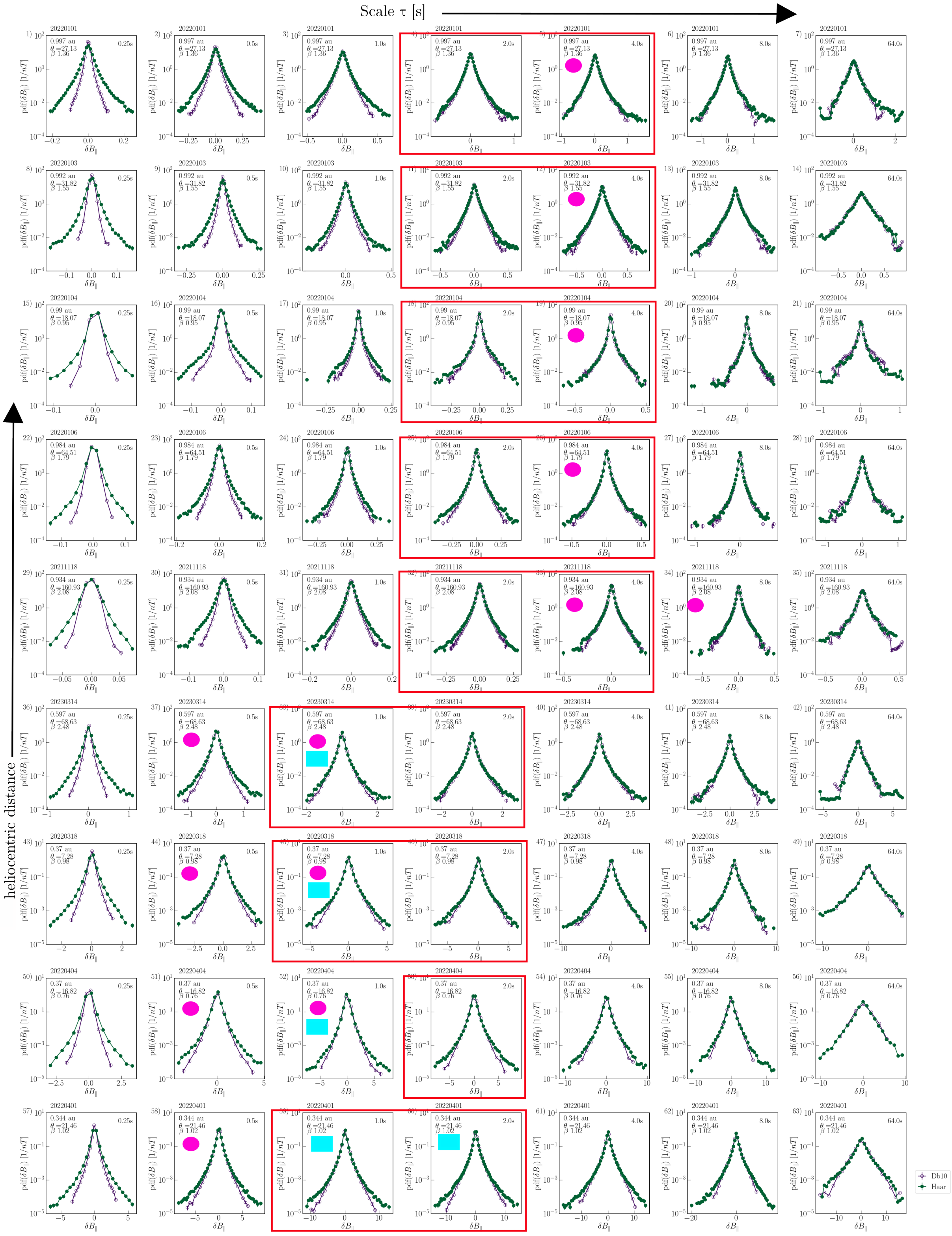

Figure A.5. Probability distribution functions of wavelet fluctuations of $B_{\|}$ of all intervals in order of decreasing heliocentric distance (top to bottom) and increasing scale (left to right). Filled green circles are obtained from the Haar wavelet, while open purple circles are from the Db10 wavelet. The red box marks the spectral break scales. The pink circles denote ρ_i and blue rectangles show d_i (if two panels are marked the respective characteristic scale is between those two scales).

Farge, M., Kevlahan, N., Perrier, V., & Goirand, E. 1996, Proceedings of the IEEE, 84, 639, doi: 10.1109/5.488705

Frisch, U. 1995, Turbulence: the legacy of A.N. Kolmogorov (Cambridge: Cambridge University Press)

Gomes, L. F., Gomes, T. F. P., Rempel, E. L., & Gama, S. 2022, Monthly Notices of the Royal Astronomical Society, stac3577, doi: 10.1093/mnras/stac3577

Greco, A., Matthaeus, W. H., Perri, S., et al. 2017, Space Science Reviews, 214, 1, doi: 10.1007/s11214-017-0435-8

Harris, C. R., Millman, K. J., van der Walt, S. J., et al. 2020, Nature, 585, 357, doi: 10.1038/s41586-020-2649-2

He, J., Tu, C., Marsch, E., & Yao, S. 2011, The Astrophysical Journal, 745, L8, doi: 10.1088/2041-8205/745/1/L8

Hnat, B., Chapman, S. C., & Rowlands, G. 2003, Physical Review E, 67, 056404, doi: 10.1103/PhysRevE.67.056404

Horbury, T. S., Forman, M. A., & Oughton, S. 2008, Physical Review Letters, 101, 175005, doi: 10.1103/PhysRevLett.101.175005

Horbury, T. S., O'Brien, H., Blazquez, I. C., et al. 2020, Astronomy & Astrophysics, 642, A9, doi: 10.1051/0004-6361/201937257

Hunter, J. D. 2007, Computing in Science & Engineering, 9, 90, doi: 10.1109/MCSE.2007.55

Iroshnikov, P. S. 1963, Astronomicheskii Zhurnal, 40, 742. https://ui.adsabs.harvard.edu/abs/1963AZh....40..742I

Katul, G., Vidakovic, B., & Albertson, J. 2001, Physics of Fluids, 13, 241, doi: 10.1063/1.1324706

Kiyani, K., Osman, K., & Chapman, S. 2015, Philosophical transactions. Series A, Mathematical, physical, and engineering sciences, 373, doi: 10.1098/rsta.2014.0155

Kiyani, K. H., Chapman, S. C., Khotyaintsev, Y. V., Dunlop, M. W., & Sahraoui, F. 2009, Physical Review Letters, 103, 075006, doi: 10.1103/PhysRevLett.103.075006

Kiyani, K. H., Chapman, S. C., Sahraoui, F., et al. 2013, The Astrophysical Journal, 763, 10, doi: 10.1088/0004-637X/763/1/10

Koga, D., Chian, A. C.-L., Miranda, R. A., & Rempel, E. L. 2007, Physical Review E, 75, 046401, doi: 10.1103/PhysRevE.75.046401

Kolmogorov, A. N., Levin, V., Hunt, J. C. R., Phillips, O. M., & Williams, D. 1997, Proceedings of the Royal Society of London. Series A: Mathematical and Physical Sciences, 434, 9, doi: 10.1098/rspa.1991.0075

Lotz, S., Nel, A. E., Wicks, R. T., et al. 2023, The Astrophysical Journal, 942, 93, doi: 10.3847/1538-4357/aca903

Mallat, S. 1989, IEEE Transactions on Pattern Analysis and Machine Intelligence, 11, 674, doi: 10.1109/34.192463

Marino, R., & Sorriso-Valvo, L. 2023, Physics Reports, 1006, 1, doi: 10.1016/j.physrep.2022.12.001

Markovskii, S. A., Vasquez, B. J., & Smith, C. W. 2008, The Astrophysical Journal, 675, 1576, doi: 10.1086/527431

Maruca, B. A., Qudsi, R. A., Alterman, B. L., et al. 2023, Astronomy & Astrophysics, 675, A196, doi: 10.1051/0004-6361/202345951

Matthaeus, W., Goldstein, M. L., & Roberts, D. A. 1990, Journal of Geophysical Research: Space Physics, 95, 20673, doi: 10.1029/JA095iA12p20673

Matthaeus, W. H., & Goldstein, M. L. 1982, Journal of Geophysical Research: Space Physics, 87, 6011, doi: 10.1029/JA087iA08p06011

Meneveau, C. 1991, Journal of Fluid Mechanics, 232, 469, doi: 10.1017/S0022112091003786

Müller, D., Marsden, R. G., St. Cyr, O. C., Gilbert, H. R., & The Solar Orbiter Team. 2013, Solar Physics, 285, 25, doi: 10.1007/s11207-012-0085-7

Müller, D., Cyr, O. C. S., Zouganelis, I., et al. 2020, Astronomy & Astrophysics, 642, A1, doi: 10.1051/0004-6361/202038467

Narasimha, R. 2007, Sadhana, 32, 29, doi: 10.1007/s12046-007-0003-0

Nickolas, P. 2017, Wavelets: A Student Guide, Australian Mathematical Society Lecture Series (Cambridge: Cambridge University Press), doi: 10.1017/9781139644280

Nicol, R. M., Chapman, S. C., & Dendy, R. O. 2008, The Astrophysical Journal, 679, 862, doi: 10.1086/586732

Osman, K., Matthaeus, W., Gosling, J., et al. 2014, Physical Review Letters, 112, 215002, doi: 10.1103/PhysRevLett.112.215002

Osman, K. T., Matthaeus, W. H., Hnat, B., & Chapman, S. C. 2012a, Physical Review Letters, 108, 261103, doi: 10.1103/PhysRevLett.108.261103

Osman, K. T., Matthaeus, W. H., Wan, M., & Rappazzo, A. F. 2012b, Physical Review Letters, 108, 261102, doi: 10.1103/PhysRevLett.108.261102

Oughton, S., Matthaeus, W. H., Wan, M., & Osman, K. T. 2015, Philosophical Transactions of the Royal Society A: Mathematical, Physical and Engineering Sciences, 373, 20140152, doi: 10.1098/rsta.2014.0152

Owen, C. J., Bruno, R., Livi, S., et al. 2020, Astronomy & Astrophysics, 642, A16, doi: 10.1051/0004-6361/201937259

Pagel, C., & Balogh, A. 2003, Journal of Geophysical Research: Space Physics, 108, SSH 2, doi: 10.1029/2002JA009498

Percival, D. B., & Walden, A. T. 2000, Wavelet Methods for Time SeriesAnalysis (Cambridge: Cambridge University Press), doi: 10.1017/CBO9780511841040

Perri, S., Goldstein, M. L., Dorelli, J. C., & Sahraoui, F. 2012, Physical Review Letters, 109, 191101, doi: 10.1103/PhysRevLett.109.191101

Podesta, J. J. 2009, The Astrophysical Journal, 698, 986, doi: 10.1088/0004-637X/698/2/986

Podesta, J. J., Roberts, D. A., & Goldstein, M. L. 2007, The Astrophysical Journal, 664, 543, doi: 10.1086/519211

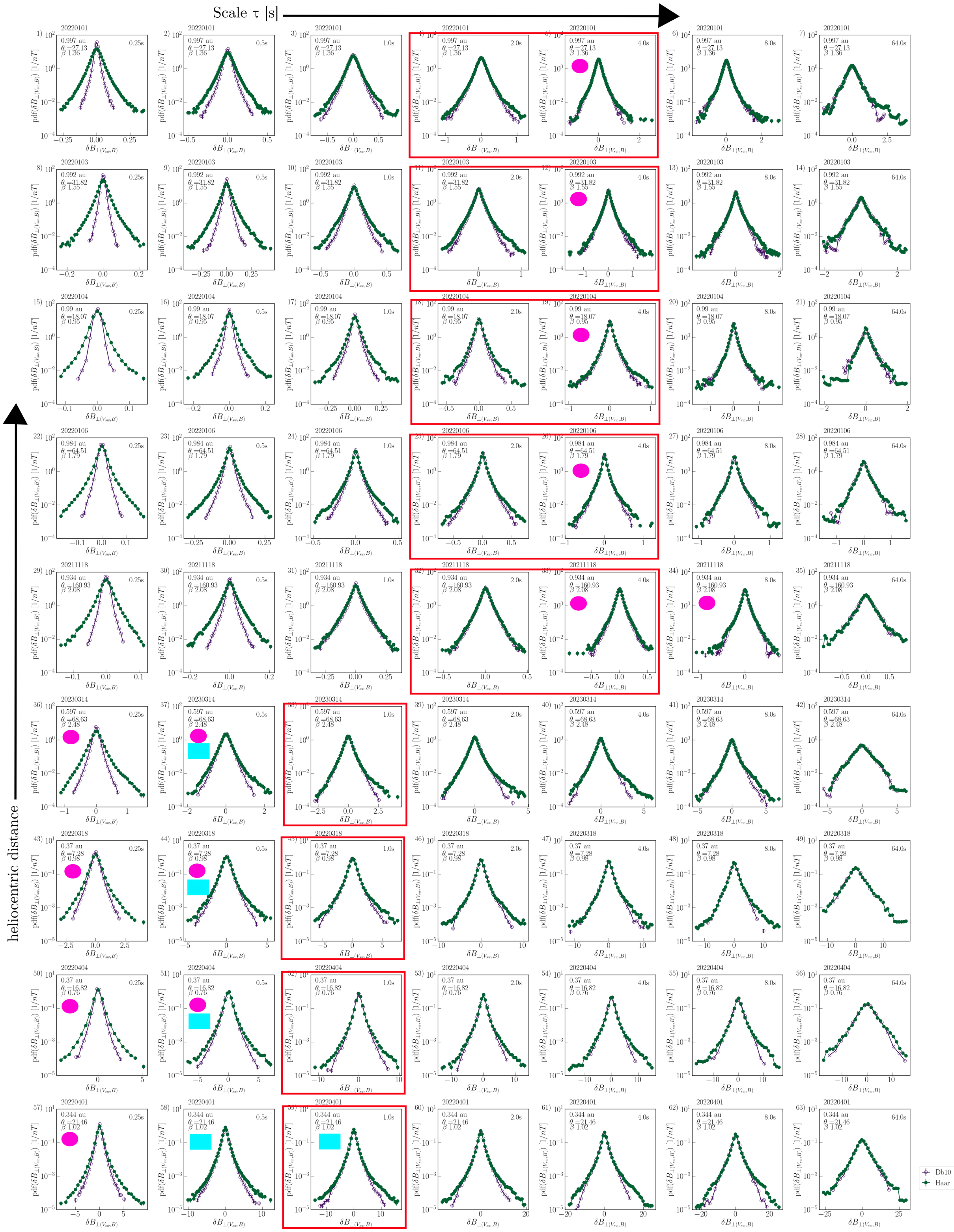

Figure A.6. Probability distribution functions of wavelet fluctuations of $B_{\perp(V_{sw},B)}$ of all intervals in order of decreasing heliocentric distance (top to bottom) and increasing scale (left to right). Filled green circles are obtained from the Haar wavelet, while open purple circles are from the Db10 wavelet. The red box marks the spectral break scales. The pink circles denote ρ_i and blue rectangles show d_i (if two panels are marked the respective characteristic scale is between those two scales).

Roberts, O., Alexandrova, O., Kajdič, P., et al. 2017, The Astrophysical Journal, 850, doi: 10.3847/1538-4357/aa93e5

Sahraoui, F., Goldstein, M. L., Robert, P., & Khotyaintsev, Y. V. 2009, Physical Review Letters, 102, 231102, doi: 10.1103/PhysRevLett.102.231102

Salem, C. S., Howes, G. G., Sundkvist, D., et al. 2012, The Astrophysical Journal Letters, 745, L9, doi: 10.1088/2041-8205/745/1/L9

Schneider, K., & Farge, M. 2001, in Wavelet Transforms and Time-Frequency Signal Analysis, ed. L. Debnath, Applied and Numerical Harmonic Analysis (Boston, MA: Birkhäuser), 181–216, doi: 10.1007/978-1-4612-0137-3_7

Sioulas, N., Velli, M., Chhiber, R., et al. 2022a, The Astrophysical Journal, 927, 140, doi: 10.3847/1538-4357/ac4fc1

Sioulas, N., Huang, Z., Velli, M., et al. 2022b, The Astrophysical Journal, 934, 143, doi: 10.3847/1538-4357/ac7aa2

Sorriso-Valvo, L., Carbone, V., Veltri, P., Consolini, G., & Bruno, R. 1999, Geophysical Research Letters, 26, 1801, doi: 10.1029/1999GL900270

Tindale, E., & Chapman, S. C. 2017, Journal of Geophysical Research: Space Physics, 122, 9824, doi: 10.1002/2017JA024412

Torrence, C., & Compo, G. P. 1998, Bulletin of the American Meteorological Society, 79, 61, doi: 10.1175/1520-0477(1998)079⟨0061:APGTWA⟩2.0.CO;2

Tu, C. Y., & Marsch, E. 1995, Space Science Reviews, 73, 1, doi: 10.1007/BF00748891

Turner, A. J., Gogoberidze, G., & Chapman, S. C. 2012, Physical Review Letters, 108, 085001, doi: 10.1103/PhysRevLett.108.085001

Veltri, P. 1999, Plasma Physics and Controlled Fusion, 41, A787, doi: 10.1088/0741-3335/41/3A/071

Verscharen, D., Klein, K. G., & Maruca, B. A. 2019, Living Reviews in Solar Physics, 16, 5, doi: 10.1007/s41116-019-0021-0

Virtanen, P., Gommers, R., Oliphant, T. E., et al. 2020, Nature Methods, 17, 261, doi: 10.1038/s41592-019-0686-2

Wang, X., Chapman, S. C., Dendy, R. O., & Hnat, B. 2023, Astronomy & Astrophysics, 678, A186, doi: 10.1051/0004-6361/202346678

Wang, X., Tu, C.-Y., He, J.-S., & Wang, L.-H. 2018, Journal of Geophysical Research: Space Physics, 123, 68, doi: 10.1002/2017JA024813

Welch, P. 1967, IEEE Transactions on Audio and Electroacoustics, 15, 70, doi: 10.1109/TAU.1967.1161901

Wicks, R. T., Horbury, T. S., Chen, C. H. K., & Schekochihin, A. A. 2010, Monthly Notices of the Royal Astronomical Society: Letters, 407, L31, doi: 10.1111/j.1745-3933.2010.00898.x

Wilk, M. B., & Gnanadesikan, R. 1968, Biometrika, 55, 1, doi: 10.1093/biomet/55.1.1

Wu, P., Perri, S., Osman, K., et al. 2013, The Astrophysical Journal Letters, 763, L30, doi: 10.1088/2041-8205/763/2/L30

Yamada, M., & Ohkitani, K. 1991a, Fluid Dynamics Research, 8, 101, doi: 10.1016/0169-5983(91)90034-G

—. 1991b, Progress of Theoretical Physics, 86, 799, doi: 10.1143/ptp/86.4.799

Yordanova, E., Balogh, A., Noullez, A., & von Steiger, R. 2009, Journal of Geophysical Research: Space Physics, 114, doi: 10.1029/2009JA014067

Zhang, J., Huang, S. Y., He, J. S., et al. 2022, The Astrophysical Journal Letters, 924, L21, doi: 10.3847/2041-8213/ac4027

Zhou, M., Liu, Z., & Loureiro, N. F. 2023, Proceedings of the National Academy of Sciences, 120, e2220927120, doi: 10.1073/pnas.2220927120

Šafránková, J., Němeček, Z., Němec, F., et al. 2023, The Astrophysical Journal Letters, 946, L44, doi: 10.3847/2041-8213/acc531

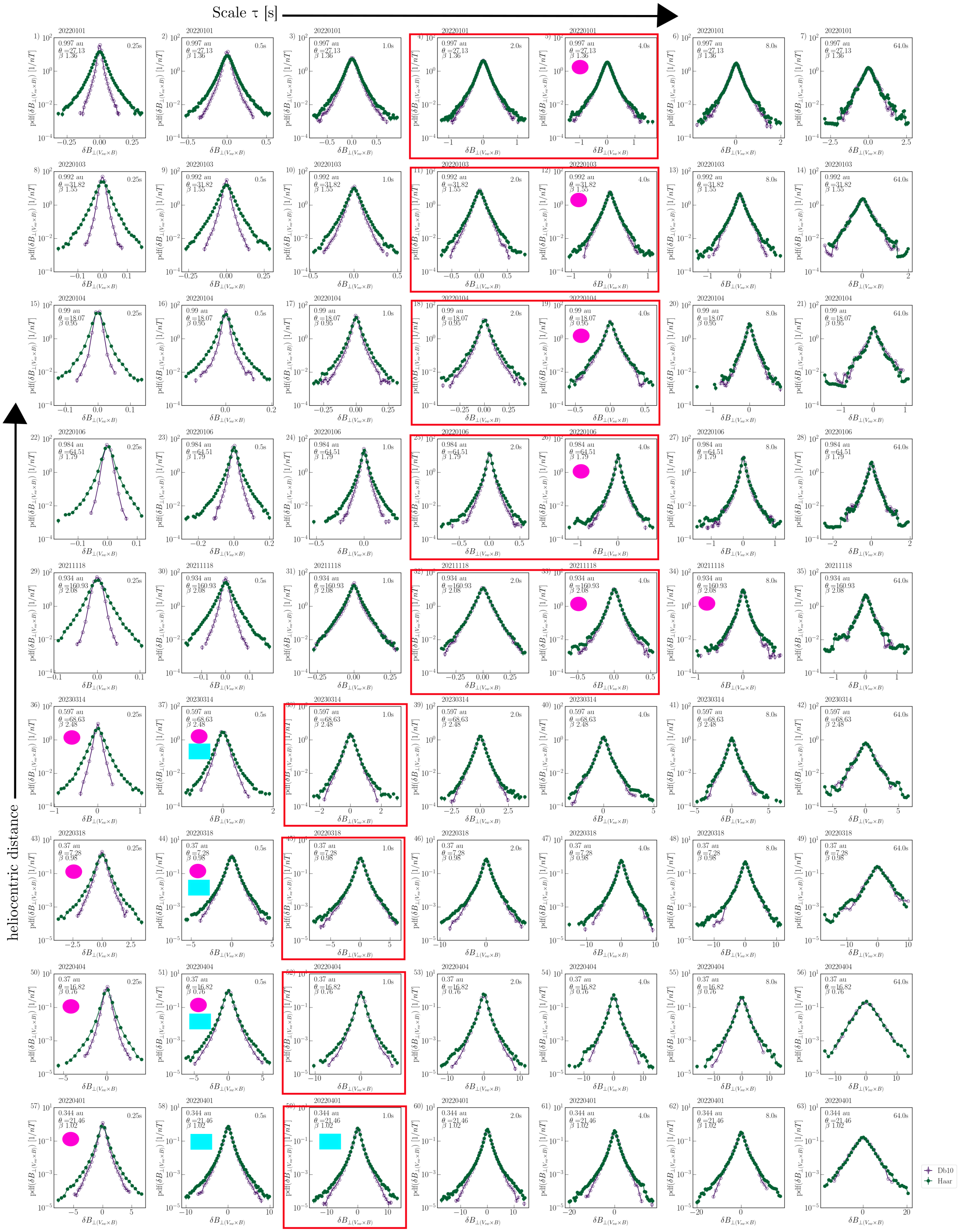

Figure A.7. Probability distribution functions of wavelet fluctuations of $B_{\perp(V_{sw}\times B)}$ of all intervals in order of decreasing heliocentric distance (top to bottom) and increasing scale (left to right). Filled green circles are obtained from the Haar wavelet, while open purple circles are from the Db10 wavelet. The red box marks the spectral break scales. The pink circles denote ρ_i and blue rectangles show d_i (if two panels are marked the respective characteristic scale is between those two scales).

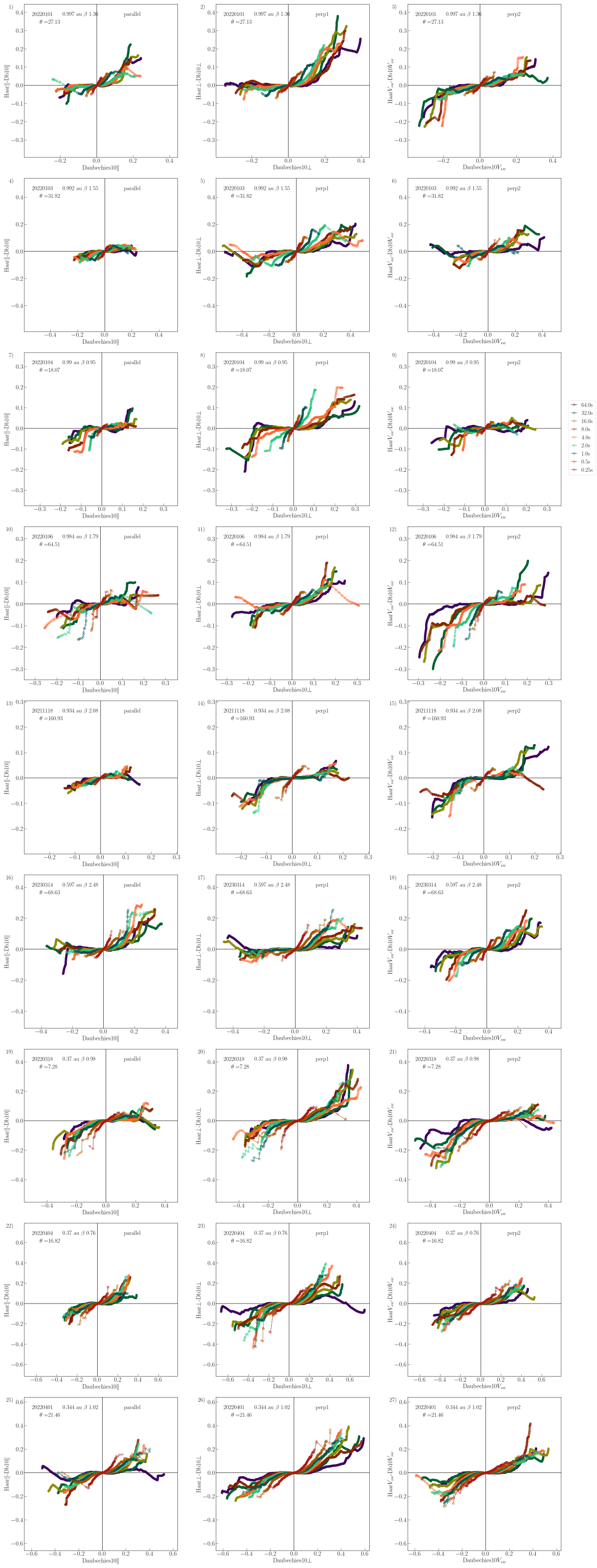

Figure A.8. QQ-Plots of the Haar wavelet details versus the daubechies 10 wavelet details overlayed per scale for all intervals (rows, also labelled at the top right corner of the panels) and all magnetic field components (columns). The different scales are denoted with different colours. Scales from 0.25 to 4 s and additionally 64 s scales are used.

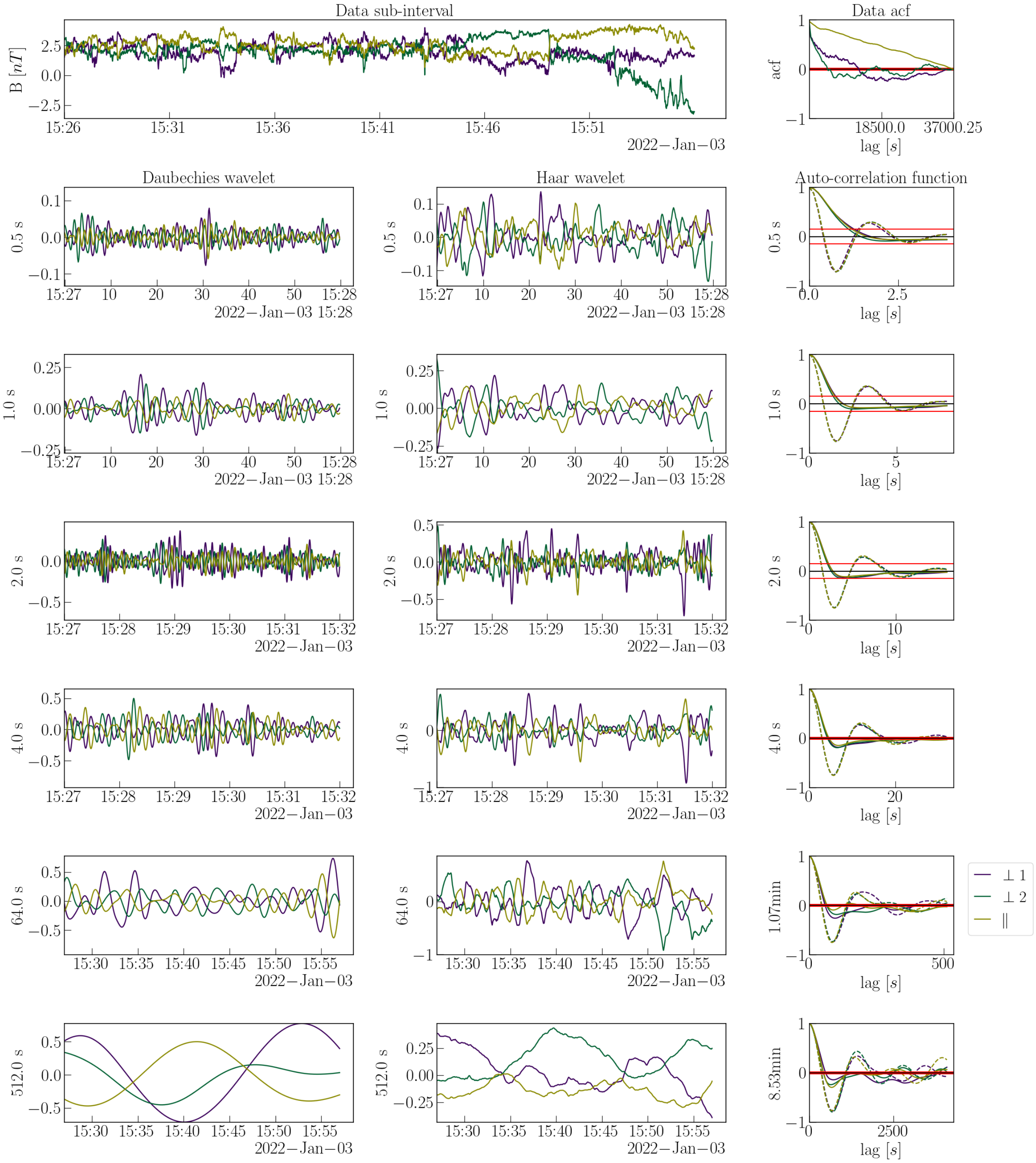

Figure A.9. Decomposition of magnetic field time-series of interval at 0.989 au from 2022-01-04 on scales 0.5 to 4 s and 64 s and 512 s of time-series (left) by Db10 and (middle) by Haar wavelet. (c) Haar wavelets. Right panels show acf of the middle third of decomposition time-series of Db10, dashed line and Haar, continuous lines. Red horizontal lines indicate the significance level obtained from auto-correlations of coloured noise with corresponding spectral exponents in the kinetic and inertial range. In purple the $B_{\perp(V_{sw},B)}$, in green the $B_{\perp(V_{sw}\times B)}$, and finally in yellow $B_{\|}$.